New Journal of Physics
The open access journal at the forefront of physics

Deutsche Physikalische Gesellschaft DPG IOP Institute of Physics International Year of Quantum Science and Technology

PAPER • OPEN ACCESS

Probing magnons with high-energy electrons: theoretical insights into spin and charge scattering in STEM-EELS

To cite this article: Julio A do Nascimento *et al* 2025 *New J. Phys.* **27** 113505

IOP Publishing New J. Phys. 27 (2025) 113505 https://doi.org/10.1088/1367-2630/ae152a

New Journal of Physics
The open access journal at the forefront of physics

Deutsche Physikalische Gesellschaft DPG
IOP Institute of Physics

Published in partnership with: Deutsche Physikalische Gesellschaft and the Institute of Physics

RECEIVED
7 July 2025

REVISED
26 September 2025

ACCEPTED FOR PUBLICATION
20 October 2025

PUBLISHED
14 November 2025

PAPER

Probing magnons with high-energy electrons: theoretical insights into spin and charge scattering in STEM-EELS

Julio A do Nascimento[1,*], Daniel M Cheshire[1], Fabrizio Cossu[1,2], Adam Kerrigan[1,5], Phil J Hasnip[1], Demie Kepaptsoglou[1,3], S A Cavill[1], Quentin M Ramasse[3,4] and Vlado K Lazarov[1,5,*]

[1] School of Physics, Engineering and Technology, University of York, York YO10 5DD, United Kingdom
[2] Department of Physics, School of Natural and Computing Sciences, University of Aberdeen, Aberdeen AB24 3UE, United Kingdom
[3] SuperSTEM, Sci-Tech Daresbury Campus, Daresbury WA4 4AD, United Kingdom
[4] School of Physics and Astronomy, University of Leeds, Leeds LS2 9JT, United Kingdom
[5] York-JEOL Nanocentre, University of York, York YO10 5BR, United Kingdom
[*] Authors to whom any correspondence should be addressed.

E-mail: julio.nascimento@york.ac.uk and vlado.lazarov@york.ac.uk

Keywords: spintronics, magnon dispersion, spin mapping, yttrium iron garnet, YIG

Abstract

In this work, we provide fundamental insights into the scattering mechanisms of non-spin-polarised electron beams with magnetic systems, as implemented in modern meV-level scanning transmission electron microscopy electron energy loss spectroscopy (STEM-EELS) instruments. We demonstrate that the charge contribution to electron-probe-magnon scattering is significant, exhibiting a near-quadratic dependence on the electron probe's momentum. This contribution can surpass spin-based interactions by orders of magnitude at higher beam acceleration voltages. Furthermore, unlike spin-based interactions, the charge-based interaction strongly depends on the relative angle between the probe's wavevector and the local magnetic moments. We derive analytical expressions for both spin-based and charge-based interactions in EELS, comparing them with established inelastic neutron scattering results and elucidating conditions under which each scattering mechanism dominates. This formalism is applied to yttrium iron garnet, a prototypical magnonic material. Our findings are crucial for guiding future experiments and data analysis in nanomagnonics, paving the way for high spatial resolution magnon spectroscopy via STEM-EELS.

1. Introduction

Current trends in information technology, such as improvements in hardware efficiency, advances in cooling systems, and a shift towards more efficient cloud and hyperscale data centers are driving the demand for scalable and energy-efficient data processing and storage solutions. The energy consumption of this sector has continued to increase significantly over the past few years [1, 14], solving this rather challenging problem drives the search for alternative technologies to meet the rising energy demand. One possible solution is the adoption of spintronics-based devices to harness the production, transmission, and processing of information using spin waves, which are dynamic Eigen-excitations of magnetically ordered materials, often described in terms of their quanta, which are termed magnons [3, 37].

The systematic investigation of the generation, manipulation and identification of magnons requires a focus on improving the methodologies for probing these phenomena. Magnons are commonly studied using inelastic neutron scattering (INS) techniques [2, 21, 27, 45], which provide meV energy resolution and the ability to probe short-wavelength magnons, albeit with poor spatial resolution [18, 58]. Time-resolved magneto-optical Kerr microscopy [29, 38, 50, 54, 55, 59] and Brillouin light scattering (BLS) [46] offer high energy resolution for probing the energy-momentum dispersion of magnons. In addition, resonant inelastic x-ray scattering (RIXS) provides momentum-resolved measurements of magnetic excitation with meV energy resolution [17, 47]. However, their spatial resolution is limited to hundreds of nanometers, and these techniques, with the exception of RIXS, are limited to long-wavelength spin waves due to the small momentum of the light sources [46, 57].

In addition to photons and neutrons as a probe for magnons, electrons have also been utilized mainly in reflection geometry, employing reflection electron energy loss spectroscopy (REELS) [60, 62]. Theoretical approaches for evaluating the electron energy loss spectra of magnons have been developed focusing on exchange-like interactions of a spin-polarised probe with the magnetic solid's local spins [15]. Furthermore, the computation of magnon electron energy loss spectroscopy (EELS) utilizing Pauli-multislice simulations has also been recently reported [7, 16, 64]. While the Pauli-multislice approach provides a powerful framework for incorporating beam properties and dynamical scattering, it inherently obscures direct insight into the explicit dependencies on the scattering vector, beam voltage, and the relative angle between the electron wavevector and local magnetic moments.

Despite these advances, a fundamental understanding of electron-spin system interactions, where electron energies are an order of magnitude higher than those in REELS, remains lacking, particularly discerning spin-spin and charge-spin interactions. Developing an analytical formalism is beneficial to meeting the growing demand for higher spatial resolution in nanomagnonics, which can be achieved via scanning transmission electron microscopy (STEM)-EELS, by guiding experiment design and data analysis. We note that high-energy electron probes (e.g. $>60\,\mathrm{keV}$) in STEM geometry have proven highly effective for quasiparticle spectroscopy. Notably, meV-resolution STEM-EELS has made significant strides in phonon spectroscopy, achieving atomic-level contrast [23], detecting spectral signatures of individual impurity atoms [24], and enabling spatial- and angle-resolved measurements of defects in crystalline materials [26].

The interaction of magnetic moments with the electron beam is weaker, compared to the Coulomb potential, by up to 3 or 4 orders of magnitude, which makes their detection challenging [33, 36]. Recently, experimental applications of meV-level STEM-EELS to directly probe magnons has been reported [30], as well for detecting magnon-phonon coupling [44]. Hence, this technique, recently demonstrated in a world-first set of experiments [30], uniquely combines the high spatial resolution needed to study exchange magnons at thin-film interfaces and defects with atomic resolution, while maintaining an energy resolution comparable to that of INS. All of this is accomplished with a significantly shorter acquisition time compared to INS and RIXS. These advances are due to recent advancements in detection technology, such as the adoption of hybrid-pixel detectors for EELS applications, which led to a drastic improvement in the detectors' dynamic range and background noise levels, allowing signals a mere 10^{-7} of the full beam intensity to be detected [42]. In addition, improved monochromator and spectrometer designs have resulted in increased energy resolution, in particular at lower acceleration voltages ($4.2\,\mathrm{meV}$ at $30\,\mathrm{kV}$ [31]).

In this work, by utilizing second quantization we evaluate the double differential cross-section to provide fundamental insights into the scattering mechanism of non-spin-polarised electron beams with magnetic systems, as implemented in modern meV-level STEM-EELS instruments, with a focus on both spin and charge contributions to the total electron-probe-magnon scattering. We show that the charge contribution is significant and has a near-quadratic dependence on the electron probe's momentum, hence can be orders of magnitude stronger than the spin-based interaction at higher beam acceleration voltages. Additionally, in contrast to spin-based interaction, we show that the charge-based interaction strongly depends on the relative angle between the probe's wavevector and the solid's local magnetic moments.

We also derive analytical expressions for spin-based and charge-based interactions in EELS, and compare the results with those of INS, a standard method for the momentum-resolved analysis of quasiparticle dispersion relations [28]. Furthermore, our work provides insights into the conditions under which either spin or charge scattering dominates.

The formalism developed in this work was applied to yttrium iron garnet ($Y_3Fe_5O_{12}$, or YIG), a prototype magnonic material, due to its exceptionally low Gilbert damping ($\approx 10^{-5}$) even in thin films [10] and electrically insulating nature [8, 52], qualities that make it an ideal foundation for spin-wave-based logic devices. Additionally, its appeal has been further increased by successful demonstrations of fast domain wall motion [6], magnetization switching and oscillation at low current densities in spin-orbit torque devices [11, 22, 61], as well as highly efficient information transfer [12, 13].

2. Methods

Given the small magnitude of the energy transfer via magnon scattering compared to the typical energy of the probe electrons, the first Born approximation can be applied. This allows us to describe the inelastic scattering probability of electrons by magnons through the double differential cross-section, as given in equation (1). It provides the relative intensity of scattered particles into a solid angle $d\Omega$, with a wave-vector within a small range around $\mathbf{k}_1$ given by $d\mathbf{k}_1$. Assuming N scatterers in the target material, and a monochromatic beam with wave-vector $\mathbf{k}_0$ in the z-direction with a particle current density $(j_0)_z$, the double differential cross-section is [35, 51]:

$$\frac{\mathrm{d}^2\sigma}{\mathrm{d}\Omega d\mathbf{k}_1} = \frac{1}{N}\frac{N_0 V\sum_{n_0,n_1,\sigma_0,\sigma_1} P_{n_0}P_{\sigma_0}k_1^2|\langle n_1,\sigma_1,\mathbf{k}_1|\hat{H}_{\text{inter}}|n_0,\sigma_0,\mathbf{k}_0\rangle|^2\delta\left(E_{n_0}+E_0-E_{n_1}-E_1\right)}{\left(2\pi\right)^2\hbar\left(j_0\right)_z}. \tag{1}$$

Here, we describe a scattering process in which the spin-system undergoes a transition from state n_0 with energy E_{n_0} to state n_1 with energy E_{n_1}.

As derived by Sturm [51], the double differential cross section depends on k_1^2. This arises from the definition of the cross-section, being a ratio of the scattered particles and incoming particles. It is defined in terms of the number of scattered particles per unit time into a solid angle $\mathrm{d}\Omega$ and energy range $\mathrm{d}E_1$. For the scattered particles, this is proportional to the number of available final states. The density of these final states, $D(k_1)$, in momentum space is given by

$$D\left(k_1\right) = V/\left(2\pi\right)^3. \tag{2}$$

When converting this to a form that depends on solid angle and energy, a volume element in k-space (d^3k_1) is used. In spherical coordinates, this volume element is $\mathrm{d}^3k_1 = k_1^2\mathrm{d}k_1\mathrm{d}\Omega$. The term for the density of states in the momentum and energy volume element becomes:

$$D\left(k_1\right)d^3k_1 = V/\left(2\pi\right)^3 k_1^2 dk_1 d\Omega, \tag{3}$$

which gives the square dependence with k_1.

Simultaneously, the scattered particle changes its state from momentum k_0 and spin σ_0 with energy E_0 to momentum k_1 and spin σ_1 with energy E_1. The interaction between the particle and the material is represented by the interaction Hamiltonian $\hat{H}_{\text{inter}}$. Here, P_{n_0} and P_{σ_0} denote the probability of the material to be in state n_0 and of the beam to be in the spin state σ_0, before any scattering event. Also, N represents the number of scatterers, N_0 is the number of particles in state k_0, and V is the volume that defines the box normalization.

The choice of the interaction Hamiltonian $\hat{H}_{\text{inter}}$ is the central point of the discussion. In our case, we are focusing on the electron beam's interaction with the system's magnetic structure. The Hamiltonian includes the interaction between the magnetic field generated by both the intrinsic magnetic moments of the electrons and the orbital angular momentum, with the probe's magnetic moment and charge, hence we can write $\hat{H}_{\text{inter}} = \hat{H}^S_{\text{inter}} + \hat{H}^C_{\text{inter}}$, where the first term takes into account the spin-based and the second the charge-based interactions.

For the spin-based interactions we note that the formalism is similar to the INS case. This approach leads to a pair of terms, an exchange-like term and a term involving the spin-orbit interaction [35]. For systems where the orbital angular momentum is negligible, only the former term is taken into account.

The charge-based interaction leads to an alteration to the electron beam's canonical momentum caused by the vector potential originating from the magnons in the magnetic solid. Below we describe in more detail how both interactions are treated in our calculations. A more detailed derivation is provided in the Supplementary Material.

2.1. Spin-based interaction

Here, the interaction between the probe's magnetic moment and the magnetic field produced by the magnetic lattice is considered [35]. In principle, both spin and orbital angular momentum give rise to the total atomic magnetic moment. We will assume the orbital angular momentum contribution to be small compared to the spin angular momentum. This assumption is valid for cases where the crystalline field quenches the orbital contribution to the total magnetic moment [4], which is a valid approximation for many 3d transition metal systems and is particularly valid in d^5 systems, where $L = 0$, which is the case for YIG [9]. This allows us to set the Landé g-factor to be purely from spin, i.e. $g_e \approx 2$. The spin of the electron beam is defined in terms of the Pauli matrices $\hat{\boldsymbol{\sigma}}$, hence the spin-based interaction is given by,

$$\hat{H}^{S}_{\text{inter}} = -\mu_B \hat{\boldsymbol{\sigma}} \cdot \mathbf{B} \tag{4}$$

where μ_B is the Bohr magneton and $\mathbf{B}$ is the sample's magnetic induction field. Given the previous assumption of purely spin magnetic moments, $\mathbf{B}$ can be written as the contribution of each magnetic moment at sites $\mathbf{r}_j$ in terms of the spin operators $\hat{S}_j$, where j labels the different lattice spins positions, giving us,

$$\hat{H}^{S}_{\text{inter}} = \frac{\mu_0 \mu_B^2}{2\pi} \hat{\boldsymbol{\sigma}} \cdot \left[\sum_j \nabla_{\mathbf{r}} \times \left(\frac{\hat{S}_j \times (\mathbf{r} - \mathbf{r}_j)}{|\mathbf{r} - \mathbf{r}_j|^3} \right) \right]. \tag{5}$$

Here, $\mathbf{r}$ is the position at which the magnetic field is measured, and $\nabla_{\mathbf{r}}$ is the vector differential operator which acts in the position vector $\mathbf{r}$. Assuming that the scattering electron does not interact with the system before and after the scattering event, i.e. no multiple scattering events, in line with the first Born approximation, we can write the total wave function as a product between a plane wave and the magnetic states,

$$|\mathbf{k}_i, \sigma_i, n_i\rangle \rightarrow |\mathbf{k}_i\rangle |\sigma_i\rangle |n_i\rangle \tag{6}$$

for $i = 0, 1$. Here, $|\mathbf{k}_i\rangle = \frac{1}{\sqrt{V}} \mathrm{e}^{-\mathrm{i}\mathbf{k}_i \cdot \mathbf{r}}$ is the state of the probing beam, while $|n_i\rangle$ represents the state of the solid, which for our purposes is only transiting between magnetic states, such that $\hat{H}_0 |n_i\rangle = E_i |n_i\rangle$ with $\hat{H}_0$ being the Heisenberg Hamiltonian.

The procedure to derive the double-differential cross-section from the interaction given in equation (5) follows the same approach as for the neutron scattering case [34, 48], giving us,

$$\frac{\mathrm{d}^2 \sigma_{SB}}{\mathrm{d}\Omega \mathrm{d}E_1} = \left(\frac{m \mu_0 \mu_B^2}{\pi \hbar^2} \right)^2 \frac{k_1}{k_0} \sum_{\alpha\beta} \mathcal{E}_{\alpha\beta} \mathcal{S}_{\alpha\beta} (\mathbf{q}, \omega) \tag{7}$$

with

$$\mathcal{E}(\tilde{\mathbf{q}}) = \begin{pmatrix} 1 - \tilde{q}_x \tilde{q}_x & -\tilde{q}_x \tilde{q}_y & -\tilde{q}_x \tilde{q}_z \\ -\tilde{q}_y \tilde{q}_x & 1 - \tilde{q}_y \tilde{q}_y & -\tilde{q}_y \tilde{q}_z \\ -\tilde{q}_z \tilde{q}_x & -\tilde{q}_z \tilde{q}_y & 1 - \tilde{q}_z \tilde{q}_z \end{pmatrix} \tag{8}$$

where the following identity is used,

$$\delta (E_{n_0} + E_0 - E_{n_1} - E_1) = \frac{1}{2\pi} \int \mathrm{e}^{\mathrm{i}(E_{n_0} - E_{n_1}) t/\hbar} \mathrm{e}^{\mathrm{i}\omega t} \mathrm{d}t \tag{9}$$

with $\omega = (E_0 - E_1)/\hbar$ [48]. The scattering vector has been defined as $\mathbf{q} = \mathbf{k}_1 - \mathbf{k}_0$, with its normalized form $\tilde{q} = \frac{\mathbf{q}}{q}$, and the spin-scattering function,

$$\mathcal{S}_{\alpha\beta} (\mathbf{q}, \omega) = \frac{1}{2\pi N} \sum_{j,j'} F_j^* (\mathbf{q}) F_{j'} (\mathbf{q}) \int \mathrm{d}t \mathrm{e}^{-\mathrm{i}\omega t} \mathrm{e}^{-\mathrm{i}\mathbf{q} \cdot (\mathbf{r}_j - \mathbf{r}_{j'})} \langle S_j^{\alpha} (0) S_{j'}^{\beta} (t) \rangle_T \tag{10}$$

where $F_j(\mathbf{q})$ and its conjugate $F_j^*(\mathbf{q})$ are the magnetic form factors. In this context $\langle S_j^{\alpha}(0) S_{j'}^{\beta}(t) \rangle_T$ can be recognized as the spin-spin correlation function.

2.2. Charge-based interaction

The interaction of the (non-spin polarised) electron beam with the magnetic sample via charge is described by starting with the Hamiltonian for the entire system, comprised of the magnetic lattice and the incoming high-energy electron [39],

$$\hat{H} = \hat{H}_0 + \frac{\left(\hat{\mathbf{p}} + e\hat{\mathbf{A}} \right)^2}{2m} - eV. \tag{11}$$

Here, $\hat{H}_0$ is the Hamiltonian for the solid, including the kinetic and potential energies of the electrons and ions in the solid. The remaining terms represent, respectively, the kinetic energy of the incoming electrons with charge e and mass m, and the interaction between the incoming high-energy electron and the ions and electrons in the solid.

The momentum operator is given by $\hat{\mathbf{p}} = -i\hbar\nabla_{\mathbf{r}}$, where $\hbar$ is the reduced Planck constant and $\nabla_{\mathbf{r}}$ is the vector differential operator with respect to the position of the incoming electron $\mathbf{r}$. Expanding the squared term in the kinetic energy, and given that in a transmission electron microscope, the electron's high momentum, and kinetic energy ensures that the magnetic field's influence on the electron's state is small enough to treat the A^2 term as negligible, and under the Coulomb gauge condition, we obtain,

$$\hat{H} = \hat{H}_0 - \frac{\hbar^2}{2m}\nabla^2 + i\frac{e\hbar}{2m}\hat{\mathbf{A}}\cdot\nabla - eV. \tag{12}$$

The third term represents the magnetic interaction of the incoming electron with the solid, which depends solely on the electron's charge, and can hence be termed a 'charge-based interaction'.

Modeling the magnetic lattice as a set of magnetic dipoles leads to the vector potential $\hat{\mathbf{A}}$ being written as,

$$\hat{A} = \frac{\mu_0}{4\pi}\sum_j \left(\hat{\boldsymbol{\mu}}_j \times \frac{\mathbf{r}-\mathbf{r}_j}{|\mathbf{r}-\mathbf{r}_j|^3}\right) \tag{13}$$

where μ_0 is the permeability of free space, and $\hat{\boldsymbol{\mu}}_j$ is the magnetic moment operator of the j'th atom. With our assumption of orbital quenching, the magnetic moment can be written in terms of the spin operators $\hat{S}$ with the relation $\hat{\boldsymbol{\mu}}_j = -2\mu_B\hat{S}$, where $\mu_B = e\hbar/2m$ is the Bohr magneton, giving us,

$$\hat{A} = -\frac{\mu_0\mu_B}{2\pi}\sum_j \left(\hat{S}_j \times \frac{\mathbf{r}-\mathbf{r}_j}{|\mathbf{r}-\mathbf{r}_j|^3}\right) \tag{14}$$

allowing us to write the third term in equation (12) as the charge-based interaction,

$$\hat{H}^C_{\text{inter}} = -i\frac{\mu_0\mu_B^2}{2\pi}\sum_j \left(\hat{S}_j \times \frac{\mathbf{r}-\mathbf{r}_j}{|\mathbf{r}-\mathbf{r}_j|^3}\right)\cdot\nabla_r. \tag{15}$$

Substituting equation (15) into Fermi's golden rule of equation (1), and following similar steps as in the spin-based interaction, taking the incoming electron beam to be along the z-direction $\mathbf{k_0} = k_{0z}\hat{z}$, we obtain,

$$\frac{\mathrm{d}^2\sigma_{CB}}{\mathrm{d}\Omega dE_1} = \left(\frac{m\mu_0\mu_B^2}{\pi\hbar^2}\right)^2 \frac{k_1 k_{0z}}{q^2}\sum_{\alpha\beta}\mathcal{E}\left(\tilde{\mathbf{q}}\right)_{\alpha\beta}\mathcal{S}_{\alpha\beta}\left(\mathbf{q},\omega\right) \tag{16}$$

with

$$\mathcal{E}\left(\tilde{\mathbf{q}}\right) = \begin{pmatrix} \tilde{q}_y\tilde{q}_y & -\tilde{q}_x\tilde{q}_y & 0 \\ -\tilde{q}_y\tilde{q}_x & \tilde{q}_x\tilde{q}_x & 0 \\ 0 & 0 & 0 \end{pmatrix} \tag{17}$$

and $\mathcal{S}_{\alpha\beta}(\mathbf{q},\omega)$ as defined in equation (10).

The derivations above show that the charge-related interaction leads to a similar form of double differential cross-section as in equation (7), but with different dependencies on the scattering vector and electron beam momentum.

The calculation of the spin-scattering function $\mathcal{S}_{\alpha\beta}(\mathbf{q},\omega)$ can be performed in a variety of ways, under the linear spin-wave approximation for bulk systems [19, 56] and thin films [40], and using atomistic spin dynamics [25]. Here, we will use the approach described in [19], where the Holstein–Primakoff transformation is used, and the bosonic creation and annihilation operators are projected on their diagonalised counterparts using the Bogoliubov transformation. Furthermore, 'Kubler's trick' [32] is used, which allows for the calculation of the magnon modes with the freedom to align the local spins in an arbitrary orientation. In this approach the spin operator in the local reference frame ($\overline{\hat{\mathbf{S}}}_j$), is connected to the laboratory reference frame ($\hat{\mathbf{S}}_j$), by the unitary matrix $\mathcal{R}_j$ which is defined such that in the local reference frame, the spin always points in the z-direction, given by,

$$\mathcal{R}_j = \begin{pmatrix} \cos\theta_j\cos\phi_j & \cos\theta_j\sin\phi_j & -\sin\theta_j \\ -\sin\phi_j & \cos\phi_j & 0 \\ \sin\theta_j\cos\phi_j & \sin\theta_j\sin\phi_j & \cos\theta_j \end{pmatrix} \tag{18}$$

such that, $\overline{\hat{\mathbf{S}}_j} = \mathcal{R}_j \cdot \hat{\mathbf{S}}_j$, where θ_j and ϕ_j are the polar and azimuthal angles, respectively, of the spins in the laboratory reference frame.

To illustrate the developed formalism, we apply it to YIG. The magnetic order in YIG is due to the exchange interactions between the Fe^{3+} ions, and it has negligible magnetic anisotropy [43]. To calculate the spin-scattering function, we will use the exchange parameters obtained from fitting INS in [43], up to the 6th nearest neighbors exchange interactions. We note that for the third nearest neighbors, there are two possibilities of exchange parameters J_{3a} and J_{3b} as seen in figure 1. These two exchange paths are dissimilar and can be distinguished due to the symmetry of the crystal when rotated about the bond vector between the neighbors. The J_{3a} exchange path exhibits a two-fold symmetry, while the J_{3b} exchange path obeys the higher D3 symmetry point group [43]. These parameters have also been recently computed within the formalism of the atomic force theorem yielding similar results [20].

For the magnetic form factor, we used the values for Fe^{3+} given in [5].

3. Results

The theoretical framework presented here has the material-specific physics entirely encapsulated within the dynamic spin-spin correlation function, $\mathcal{S}_{\alpha\beta}(\mathbf{q},\omega)$. While we have calculated this function using a localized Heisenberg model, which is the physically appropriate description for an insulator like YIG, our formalism is readily applicable to metallic systems. For such cases, it is a standard and well-justified approach to calculate $\mathcal{S}_{\alpha\beta}(\mathbf{q},\omega)$ using an effective Heisenberg model, where the exchange parameters are derived from first-principles electronic structure calculations that account for the itinerant nature of the electrons [49, 53, 63].

Having established the generality of our framework, we now turn to the specific interactions it describes. The distinctions between the spin and charge-based interactions stem from their dependence on three factors: the scattering vector $\mathbf{q}$, the variation in intensity relative to the angle between the beam's orientation and that of the local magnetic moments, and primarily, the dependence on the beam's momentum $\mathbf{k}_0$. To further compare the momentum dependence of the spin-based $f_{\mathrm{SB}}(q,k_0)$ and charge-based interactions $f_{\mathrm{CB}}(q,k_0)$, we rewrite them in terms of the incident beam wavevector (k_0) and scattering vector (q), using the relation $q = k_1 - k_0$.

$$\begin{cases} f_{\mathrm{SB}}(q,k_0) = \frac{q+k_0}{k_0} \\ f_{\mathrm{CB}}(q,k_0) = \frac{k_0}{q} + \frac{k_0^2}{q^2}. \end{cases} \tag{19}$$

We visually compare equations (19) for q and k_0 in figure 2. As in the inelastic scattering of electrons by phonons [41], the charge-related magnon scattering function exhibits an overall stronger q^{-2} dependence. The spin-based scattering function, on the other hand, simplifies to $f_{\mathrm{SB}}(q,k_0) \approx 1$ for the typical scattering regime where $q \ll k_0$. Comparing the two, suggests that the magnon EELS signal will be strongest in the first Brillouin zone for the charge-based interaction, in contrast to spin-based interactions, which will display a stronger signal at larger q, where large in this context is scaled by k_0. However, we also note that the magnetic form factor is also q-dependent, hence the overall variation depends on the degree of ionicity in the crystal [5].

The most significant difference lies in their dependence on the beam's momentum. For high-energy electrons, such as those used in a transmission electron microscope, where k_0 is large, the term k_0^2/q^2 in the charge-based interaction will overwhelmingly dominate. This quadratic dependence ensures that at the high acceleration voltages typical of modern STEM-EELS, the charge-based interaction is the dominant scattering mechanism. This high-energy regime is not only crucial for these experiments but also fundamentally distinguishes them from earlier implementations of magnon REELS, which operated at considerably lower acceleration voltages. We note that the two terms in $f_{\mathrm{CB}}(q,k_0)$ would be of similar magnitude only in a regime where the ratio k_0/q approaches unity, which corresponds to either a very low accelerating voltage or a very large momentum transfer.

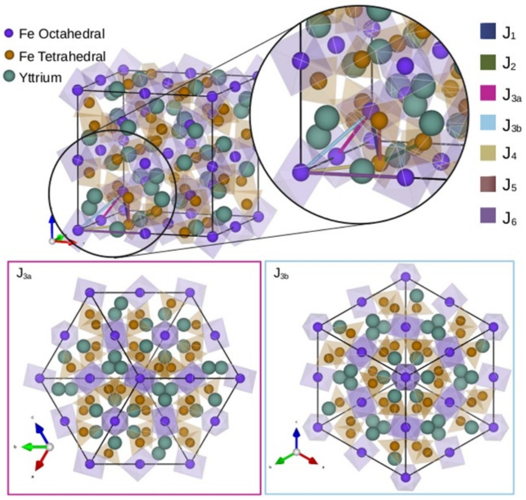

Figure 1. Crystal structure and magnetic exchange paths in yttrium iron garnet (YIG). The conventional unit cell of YIG is represented, with the majority tetrahedral sites marked in mustard and the minority octahedral sites in purple. Yttrium is depicted in teal color, and the vertices of the polyhedra implicitly represent oxygen. The first octant of the YIG unit cell is highlighted, showing the two distinct Fe^{3+} sites and their exchange paths. The bottom panels represent the dissimilar two-fold J_{3a}, and D3 J_{3b} symmetries for the third nearest neighbors.

In figure 3 we compare the magnon EELS momentum dispersion diagram of YIG for the spin-based term using equation (7) and the charge-based contribution using equation (16). The color bar intensity is given in terms of the interaction coupling constant $\left(\frac{m\mu_o\mu_B^2}{\hbar^2\pi}\right)^2$, for 200 keV electrons. We note 200 kV is a standard high acceleration voltage for STEM machines. The calculated EELS spectra reproduce the key features of the experimental INS data in reference [43] (cf figure 2(f)), particularly that the same modes are active and, as expected, the spin-based component also follows the same intensity relative to q as INS. The chosen scattering path [HHH] highlights the distinction between the two scattering mechanisms. Owing to its dependence on momentum transfer q, the charge-based interaction is dominant at and near the zone center, but its intensity diminishes rapidly with increasing q. Conversely, the spin-based interaction allows for the magnons to be observed clearly at larger scattering vectors, where the charge contribution is suppressed. However, the charge-based component contains a prefactor dependent on the incident electron momentum, k_0, which is large for high acceleration voltages. Consequently, this interaction remains significant even at higher scattering vectors q, note the color bar scale. Under the previous discussion, note that both the intensities given in the figures 3(a) and (b) coexist in the EELS spectra.

Furthermore, we note that the spin-scattering function $\mathcal{S}_{\alpha\beta}(\mathbf{q},\omega)$ is linearly dependent on the Bose–Einstein distribution [19, 40]. This implies that magnon creation is influenced by the existing magnon population, leading to increased EELS peak intensity at higher magnon densities. This suggests that, on top of thermally produced magnons, an externally pumped spin wave, generated via methods such as microwave excitation, spin-transfer torque, or an optical pump, would lead to a momentum-dependent intensity change, particularly at small scattering vector q and energies.

In all previous discussions, using the definition of the spin orientation given in equation (18), we set the magnetic moments to align parallel to the z-axis by setting $\theta = 0$ and $\phi = 0$, with the electron beam also directed along the z-axis.

Next, we discuss the intensity dependence of the relative orientation of the beam wavevector and the local magnetic moments. We evaluate the EELS for the path $N - \Gamma - H$ keeping $\phi = 0$ and varying the value of θ for an electron beam of 200 keV. For the spin-based interaction shown in figure 4 the effect of changing the relative angle between the probe wavevector and the local magnetic moments is small. The intensity change is captured by the interplay of $\mathcal{E}(\tilde{\mathbf{q}})$ given in equation (8) and the spin scattering $\mathcal{S}(\mathbf{q},\omega)$, the components of which are modulated by the relative orientation between the probe and the magnetic moments.

In contrast, we see a strong dependence on the magnetic moment's orientation in the charge-based interaction as shown in figure 5. In this context, we show a large dependence of the scattering intensity along the path $\Gamma - H$ as a function of the polar angle of the magnetic moments. This observation underscores the influence of magnetic moment alignment on the scattering process. We can also see that

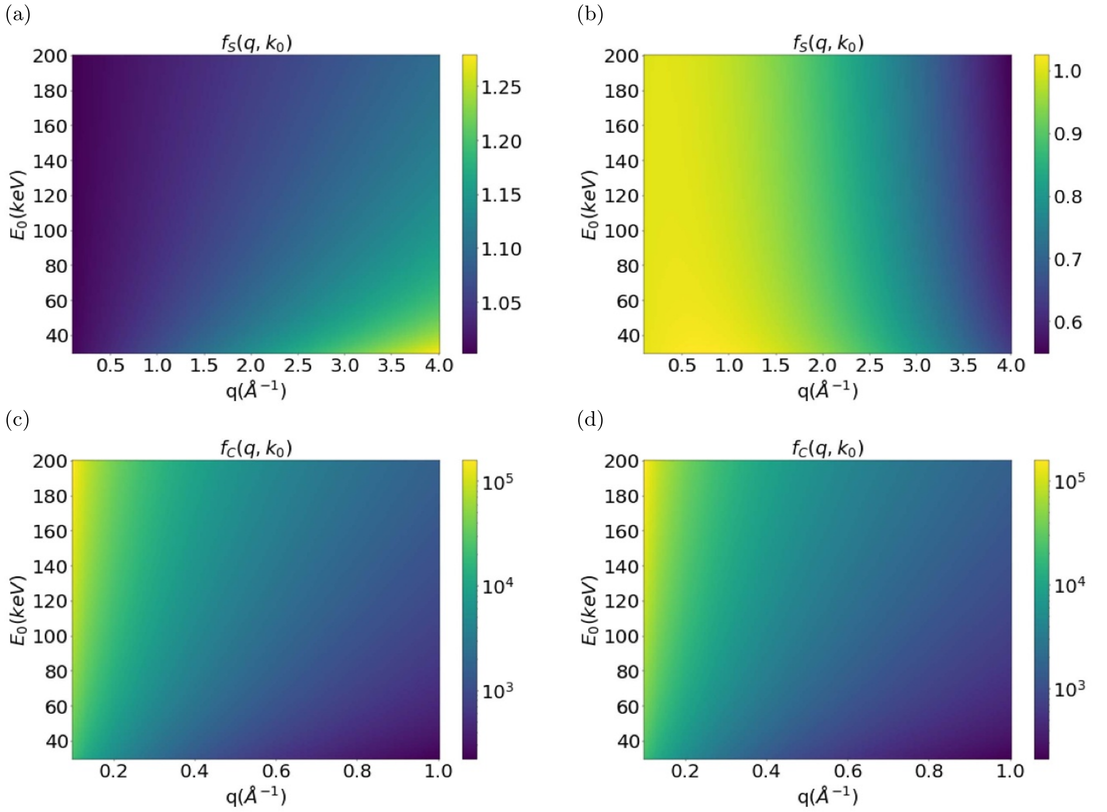

Figure 2. Cross-section dependence with the scattering vector q and incoming electron beam energy E_0 is shown for (a) spin-based interaction, (b) spin-based interaction taking the magnetic form factor for Fe^{+3} into account, (c) charge-based interaction and (d) charge-based interaction taking the magnetic form factor for Fe^{3+} into account. Color bar intensity is given in terms of $\left(\frac{m\mu_o\mu_B^2}{\hbar^2\pi}\right)^2$.

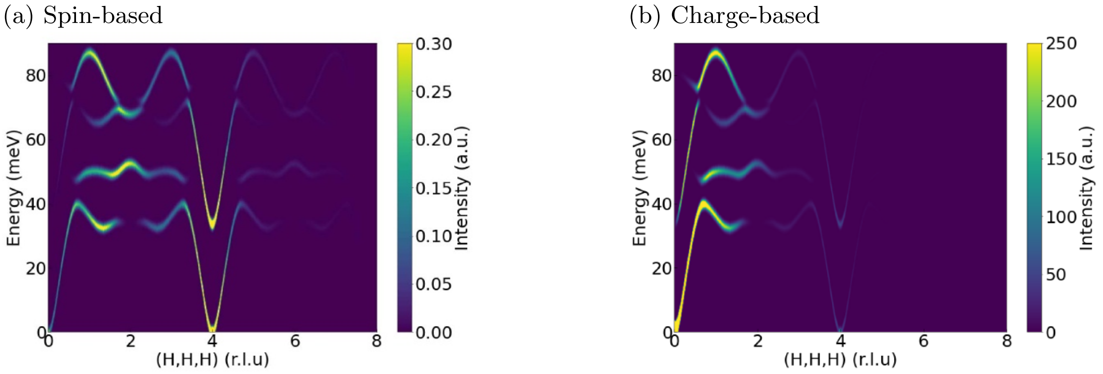

Figure 3. Inelastic scattering by magnons: (a) theoretical evaluation of spin-based EELS, (b) charge-based EELS. All the calculations were performed for a relative angle between the probe's wave vector and the magnetic moment vector orientation, $\theta = 0$. Color bar intensity is given in terms of $\left(\frac{m\mu_o\mu_B^2}{\hbar^2\pi}\right)^2$, for an acceleration voltage of 200 keV.

the intensity varies with a cosine squared relation with the angle between the magnetic moments' orientation and the beam wavevector. This property can be potentially useful to probe the magnetization direction change at nm scale, opening possibilities to study spin-structures at surfaces and interfaces, as well as topological spin-structures.

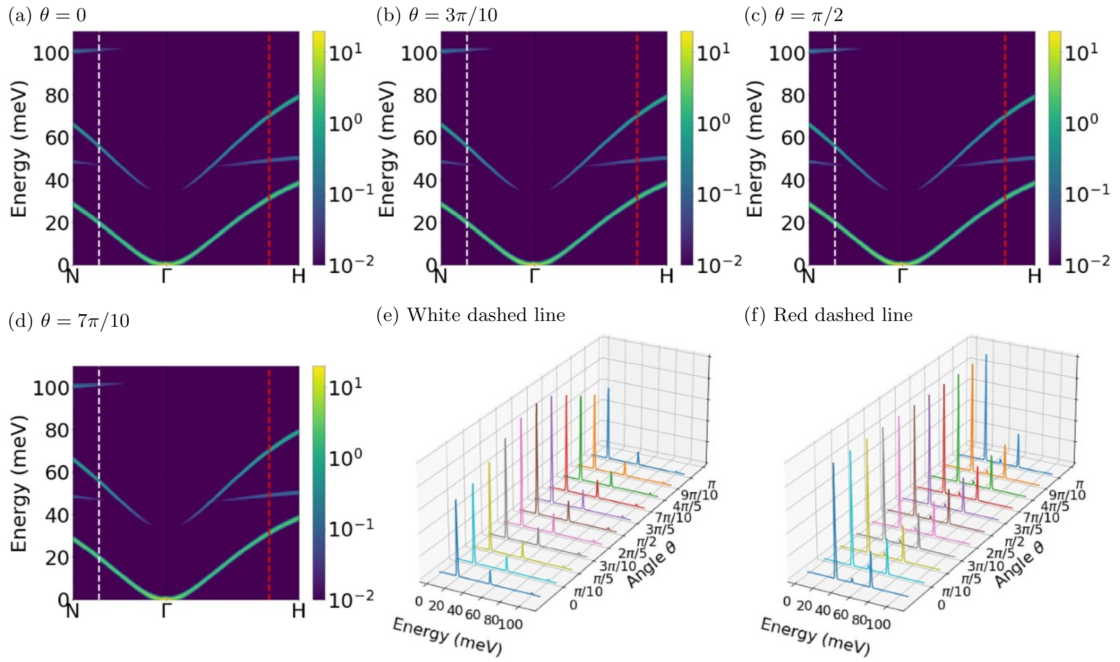

(a) $\theta = 0$ (b) $\theta = 3\pi/10$ (c) $\theta = \pi/2$

(d) $\theta = 7\pi/10$ (e) White dashed line (f) Red dashed line

Figure 4. (a)–(d) Spin-related EELS, for varying relative angles θ between the probe's wave vector and the magnetic moment vector orientation, for an acceleration voltage of 200 keV. (e)–(f) Angle-dependent intensity for the points in momentum space represented by the white and red dashed lines, showing a weak angle dependence on the point represented by the red and white dashed lines.

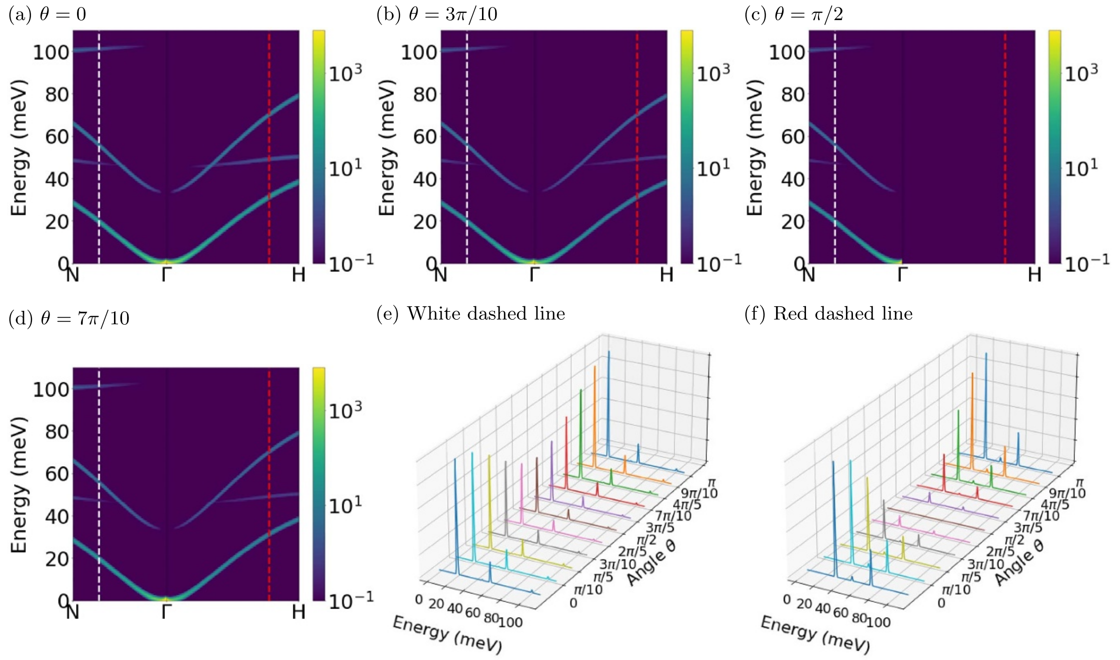

(a) $\theta = 0$ (b) $\theta = 3\pi/10$ (c) $\theta = \pi/2$

(d) $\theta = 7\pi/10$ (e) White dashed line (f) Red dashed line

Figure 5. (a)–(d) Charge-related EELS, varying relative angles θ between the probe's wave vector and the magnetic moment vector orientation. (e)–(f) Angle-dependent intensity for a particular point in momentum space, showing a strong angle dependence on the point represented by the red dashed line (f), but not on the point represented by the white dashed line (e).

4. Conclusion

In this work, we have shown that non-spin polarised electron probes can be a powerful tool for probing magnons in addition to neutrons. We provide physical insights into electron-magnon scattering by quantifying the theoretical EELS, considering separately the spin-based interaction and charge-based interaction. We reveal contrasting behavior where the charge-based interaction exhibits a quadratic dependence on the beam momentum k_0, while the spin-based interaction follows an inverse relationship k_0^{-1}, similar to phonons. Conversely, the charge-based interaction shows the same q^{-2} dependence with the scattering vector as in the case of phonons, a relation not present in the spin-based interaction. This relation points to a possible enhancement of the magnon-related peaks in contrast to the phonon-related peaks for higher acceleration voltages. In addition, the high spatial resolution nature of the STEM-EELS probe, together with the magnetic moment orientation sensitive nature of the non-spin polarised EELS spectrum, offers prospects to probe local differences in the orientation of the Curie/Néel vector relative to the electron beam momentum. In summary, our study contributes to a deeper understanding of electron-matter interactions offering insights for the design and interpretation of experiments aimed at probing the magnetic properties of materials at the nanoscale utilizing modern STEM-EELS techniques.

Supplementary material

See supplementary material for the detailed derivation of the double-differential cross-section for both spin- and charge-based interactions.

Data availability statement

All data that support the findings of this study are included within the article (and any supplementary files).

Acknowledgments

This project was undertaken on the Viking Cluster, which is a high-performance computing facility provided by the University of York. We are grateful for computational support from the University of York High-Performance Computing service, Viking and the Research Computing team. SuperSTEM is the National Research Facility for Advanced Electron Microscopy supported in part by the Engineering and Physical Sciences Research Council (EPSRC) under Grant Number EP/W021080/1.The authors acknowledge further financial support from the EPSRC via Grant Numbers EP/V048767/1, EP/Z531194/1, EP/V036432/1, as well as the Royal Society via Grant No. IES/R1/211016.

ORCID iDs

Julio A do Nascimento 0000-0002-2862-1875
Daniel M Cheshire 0000-0002-0117-1982
Fabrizio Cossu 0000-0002-8233-9117
Adam Kerrigan 0000-0001-8222-841X
Phil J Hasnip 0000-0002-4314-4093
Demie Kepaptsoglou 0000-0003-0499-0470
S A Cavill 0000-0002-1359-4958
Quentin M Ramasse 0000-0001-7466-2283
Vlado K Lazarov 0000-0002-4314-6865

References

[1] Data growth worldwide 2010-2025 (available at: www.statista.com/statistics/871513/worldwide-data-created/) (Accessed 24 February 2024)

[2] Antonini B and Minkiewicz V 1972 Neutron scattering study of spin waves and phonons in MNPT3 *Solid State Commun.* **10** 203–6

[3] Barman A *et al* 2021 The 2021 magnonics roadmap *J. Phys.: Condens. Matter* **33** 413001

[4] Blundell S 2001 *Magnetism in Condensed Matter* 1st edn (Oxford Academic) pp 94–95

[5] Brown P Magnetic form factors (available at: www.ill.eu/sites/ccsl/ffacts/)

[6] Caretta L, Oh S-H, Fakhrul T, Lee D-K, Lee B H, Kim S K, Ross C A, Lee K-J and Beach G S D 2020 Relativistic kinematics of a magnetic soliton *Science* **370** 1438–42

[7] Castellanos-Reyes J A, Zeiger P, Bergman A, Kepaptsoglou D, Ramasse Q M, Idrobo J C and Rusz J 2023 Unveiling the impact of temperature on magnon diffuse scattering detection in the transmission electron microscope *Phys. Rev. B* **108** 134435

[8] Cherepa V, Kolokolov I and L'vov V 1993 The saga of YIG: spectra, thermodynamics, interaction and relaxation of magnons in a complex magnet *Phys. Rep.* **229** 81–144
[9] Cheshire D, Bencok P, Gianolio D, Cibin G, Lazarov V K, van der Laan G and Cavill S A 2022 Absence of spin-mixed states in ferrimagnet yttrium iron garnet *J. Appl. Phys.* **132** 103902
[10] Cheshire D M, Nascimento J A D, Lazarov V K and Cavill S A 2024 Enhanced magnon transport through an amorphous magnetic insulator *Phys. Rev. B* **109** 134432
[11] Collet M *et al* 2016 Generation of coherent spin-wave modes in yttrium iron garnet microdiscs by spin-orbit torque *Nat. Commun.* **7** 10377
[12] Cornelissen L J, Liu J, Duine R A, Youssef J B and van Wees B J 2015 Long-distance transport of magnon spin information in a magnetic insulator at room temperature *Nat. Phys.* **11** 1022–6
[13] Cornelissen L J, Liu J, van Wees B J and Duine R A 2018 Spin-current-controlled modulation of the magnon spin conductance in a three-terminal magnon transistor *Phys. Rev. Lett.* **120** 097702
[14] Dokic B L 2013 A review on energy efficient CMOS digital logic *Eng. Technol. Appl. Sci. Res.* **3** 552–61
[15] dos Santos F J, dos Santos Dias M, Guimarães F S M, Bouaziz J and Lounis S 2018 Spin-resolved inelastic electron scattering by spin waves in noncollinear magnets *Phys. Rev. B* **97** 024431
[16] Edström A, Lubk A and Rusz J 2019 Quantum mechanical treatment of atomic-resolution differential phase contrast imaging of magnetic materials *Phys. Rev. B* **99** 174428
[17] Elnaggar H, Nag A, Haverkort M W, Garcia-Fernandez M, Walters A, Wang R-P, Zhou K-J and de Groot F 2023 Magnetic excitations beyond the single- and double-magnons *Nat. Commun.* **14** 2749
[18] Fernandez-Alonso F and Price D 2013 *Neutron Scattering Experimental Methods in the Physical Sciences* (Academic)
[19] Fishman R S *et al* 2018 *Spin-Wave Theory and its Applications to Neutron Scattering and THz Spectroscopy* (Morgan and Claypool Publishers) pp 2053–571
[20] Gorbatov O I, Johansson G, Jakobsson A, Mankovsky S, Ebert H, Di Marco I, Minár J and Etz C 2021 Magnetic exchange interactions in yttrium iron garnet: a fully relativistic first-principles investigation *Phys. Rev. B* **104** 174401
[21] Guggenheim H J, Hutchings M T and Rainford B D 1968 Neutron-scattering determination of spin-wave dispersion relations in FeF_2 *J. Appl. Phys.* **39** 1120–1
[22] Guo C Y, Wan C H, Zhao M K, Wu H, Fang C, Yan Z R, Feng J F, Liu H F and Han X F 2019 Spin-orbit torque switching in perpendicular $Y_3Fe_5O_{12}$/Pt bilayer *Appl. Phys. Lett.* **114** 192409
[23] Hage F S, Kepaptsoglou D M, Ramasse Q M and Allen L J 2019 Phonon spectroscopy at atomic resolution *Phys. Rev. Lett.* **122** 016103
[24] Hage F S, Radtke G, Kepaptsoglou D M, Lazzeri M and Ramasse Q M 2020 Single-atom vibrational spectroscopy in the scanning transmission electron microscope *Science* **367** 1124–7
[25] Hellsvik J, Thonig D, Modin K, Iuşan D, Bergman A, Eriksson O, Bergqvist L and Delin A 2019 General method for atomistic spin-lattice dynamics with first-principles accuracy *Phys. Rev. B* **99** 104302
[26] Hoglund E R *et al* 2022 Emergent interface vibrational structure of oxide superlattices *Nature* **601** 556–61
[27] Holbein S, Steffens P, Biesenkamp S, Ollivier J, Komarek A C, Baum M and Braden M 2023 Spin-wave dispersion and magnon chirality in multiferroic $TbMnO_3$ *Phys. Rev. B* **108** 104404
[28] Hudson B S 2001 Inelastic neutron scattering: a tool in molecular vibrational spectroscopy and a test of *ab initio* methods *J. Phys. Chem. A* **105** 3949–60
[29] Keatley P S, Loughran T H J, Hendry E, Barnes W L, Hicken R J, Childress J R and Katine J A 2017 A platform for time-resolved scanning Kerr microscopy in the near-field *Rev. Sci. Instrum.* **88** 123708
[30] Kepaptsoglou D *et al* 2025 Magnon spectroscopy in the electron microscope *Nature* **644** 83–88
[31] Krivanek O, Dellby N, Hachtel J, Idrobo J-C, Hotz M, Plotkin-Swing B, Bacon N, Bleloch A, Corbin G, Hoffman M, Meyer C and Lovejoy T 2019 Progress in ultrahigh energy resolution eels *Ultramicroscopy* **203** 60–67
[32] Kubler J, Hock K H, Sticht J and Williams A R 1988 Density functional theory of non-collinear magnetism *J. Phys. F: Met. Phys.* **18** 469–83
[33] Loudon J C 2012 Antiferromagnetism in NiO observed by transmission electron diffraction *Phys. Rev. Lett.* **109** 267204
[34] Lovesey S W 1984 Theory of neutron scattering from condensed matter *Polarization Effect and Magnetic Scattering* vol 2
[35] Lovesey S W 1984 *Theory of Neutron Scattering From Condensed Matter Volume II: Polarization Effects and Magnetic Scattering* (Clarendon)
[36] Lyon K, Bergman A, Zeiger P, Kepaptsoglou D, Ramasse Q M, Idrobo J C and Rusz J 2021 Theory of magnon diffuse scattering in scanning transmission electron microscopy *Phys. Rev. B* **104** 214418
[37] Mahmoud A, Ciubotaru F, Vanderveken F, Chumak A V, Hamdioui S, Adelmann C and Cotofana S 2020 Introduction to spin wave computing *J. Appl. Phys.* **128** 161101
[38] Mansfeld S, Topp J, Tens K, Toedt J N, Hansen W, Heitmann D and Mendach S 2012 Spin wave diffraction and perfect imaging of a grating *Phys. Rev. Lett.* **108** 047204
[39] Mendis B 2022 Quantum theory of magnon excitation by high energy electron beams *Ultramicroscopy* **239** 113548
[40] Nascimento J A D, Kerrigan A, Cavill S A, Hasnip P J, Kepaptsoglou D, Ramasse Q M and Lazarov V K 2024 Confined magnon dispersion in ferromagnetic and antiferromagnetic thin films in a second quantization approach: the case of fe and nio *Phys. Rev. B* **110** 024410
[41] Nicholls R J, Hage F S, McCulloch D G, Ramasse Q M, Refson K and Yates J R 2019 Theory of momentum-resolved phonon spectroscopy in the electron microscope *Phys. Rev. B* **99** 094105
[42] Plotkin-Swing B *et al* 2020 Hybrid pixel direct detector for electron energy loss spectroscopy *Ultramicroscopy* **217** 113067
[43] Princep A J, Ewings R A, Ward S, Tóth S, Dubs C, Prabhakaran D and Boothroyd A T 2017 The full magnon spectrum of yttrium iron garnet *npj Quantum Mater.* **2** 63
[44] Reifsnyder A, Nawwar M, Zhu M, Hachtel J A, Heremans J and McComb D W 2024 Detecting magnon-phonon coupling in the scanning transmission electron microscope *Microsc. Microanal.* **30** ozae044.772
[45] Riste T, Blinowski K and J 1959 Spin fluctuation scattering of neutrons in magnetite *J. Phys. Chem. Solids* **9** 153–64
[46] Sebastian T, Schultheiss K, Obry B, Hillebrands B and Schultheiss H 2015 Micro-focused Brillouin light scattering: imaging spin waves at the nanoscale *Front. Phys.* **3** 1–23
[47] Shrestha S *et al* 2025 Tunable magnons of an antiferromagnetic Mott insulator via interfacial metal-insulator transitions *Nat. Commun.* **16** 3592
[48] Squires G L 2012 *Introduction to the Theory of Thermal Neutron Scattering* (Cambridge University Press)

[49] Stepa E, Brener S, Krien F, Harland M, Lichtenstein A and Katsnelson M 2018 Effective Heisenberg model and exchange interaction for strongly correlated systems *Phys. Rev. Lett.* **121**

[50] Stigloher J *et al* 2016 Snell's law for spin waves *Phys. Rev. Lett.* **117** 037204

[51] Sturm K 1993 Dynamic structure factor: an introduction *Z. Naturf. A* **48** 233–42

[52] Sun Y, Song Y-Y, Chang H, Kabatek M, tz M, Schneider W, Wu M, Schultheiss H and Hoffmann A 2012 Growth and ferromagnetic resonance properties of nanometer-thick yttrium iron garnet films *Appl. Phys. Lett.* **101** 152405

[53] Szilva A, Kvashnin Y, Stepa E A, Nordström L, Eriksson O, Lichtenstein A I and Katsnelson M I 2023 Quantitative theory of magnetic interactions in solids *Rev. Mod. Phys.* **95** 035004

[54] Tamaru S, Bain J A, van de Veerdonk R J M, Crawford T M, Covington M and Kryder M H 2004 Measurement of magnetostatic mode excitation and relaxation in permalloy films using scanning Kerr imaging *Phys. Rev. B* **70** 104416

[55] Toedt J-N, Mundkowski M, Heitmann D, Mendach S and Hansen W 2016 Design and construction of a spin-wave lens *Sci. Rep.* **6** 33169

[56] Toth S and Lake B 2015 Linear spin wave theory for single-q incommensurate magnetic structures *J. Phys.: Condens. Matter* **27** 166002

[57] van Kampen M, Jozsa C, Kohlhepp J T, LeClair P, Lagae L, de Jonge W J M and Koopmans B 2002 All-optical probe of coherent spin waves *Phys. Rev. Lett.* **88** 227201

[58] Vogel S C 2013 A review of neutron scattering applications to nuclear materials *Int. Scholarly Res. Not.* **2013** 302408

[59] Wessels P, Vogel A, Tödt J-N, Wieland M, Meier G and Drescher M 2016 Direct observation of isolated Damon-Eshbach and backward volume spin-wave packets in ferromagnetic microstripes *Sci. Rep.* **6** 22117

[60] Wilkes J, Palmer R and Willis R 1987 Phonons in graphite studied by eels *J. Electron Spectrosc. Relat. Phenom.* **44** 355–60

[61] Yang M *et al* 2024 Highly efficient field-free switching of perpendicular yttrium iron garnet with collinear spin current *Nat. Commun.* **15** 3201

[62] Zakeri K, Zhang Y and Kirschner J 2013 Surface magnons probed by spin-polarized electron energy loss spectroscopy *J. Electron Spectrosc. Relat. Phenom.* **189** 157–63

[63] Zhang H-Y and Xu N 2017 Magnetic excitations in the normal and nematic phases of iron pnictides *J. Phys.: Condens. Matter* **29** 195601

[64] Ángel Castellanos-Reyes J, Zeiger P and Rusz J 2025 Dynamical theory of angle-resolved electron energy loss and gain spectroscopies of phonons and magnons in transmission electron microscopy including multiple scattering effects *Phys. Rev. Lett.* **134** 036402